Microstructures and mechanical properties of ultrafine grained 7075 Al alloy processed by ECAP and their evolutions during annealing

Y.H. Zhao [a,*], X.Z. Liao [a], Z. Jin [b], R.Z. Valiev [c], Y.T. Zhu [a,*]

[a] Materials Science and Technology Division, Los Alamos National Laboratory, MS G755, MST-STC, Los Alamos, NM 87545, USA
[b] Alcoa Technical Center, Alcoa Center, PA 15069, USA
[c] Institute of Physics of Advanced Materials, Ufa State Aviation Technical University, 12 K. Marx Street, 450000 Ufa, Russian Federation

Abstract

Microstructures and mechanical properties of equal-channel angular pressing (ECAP) processed and naturally aged ultrafine grained (UFG) and coarse grained (CG) 7075 Al alloys as well as their evolutions during annealing were investigated. After the same natural aging, the tensile yield strength, ultimate strength, and microhardness of the UFG samples were 103%, 35%, and 48% higher, respectively, than those of the CG samples, because of higher densities of Guinier–Preston (G–P) zones and dislocations in the UFG sample. Upon annealing, the microhardness of the UFG sample decreased gradually, while a hardening peak appeared for the CG sample. The peak was caused by the precipitation hardening of the metastable η' phase. For the UFG sample, the precipitation hardening was overcompensated by the significant decrease of microstrain (dislocation density) upon annealing, resulting in a lack of precipitation hardening peak. Differential scanning calorimetry indicates that the ECAP process only accelerated the phase precipitations, but did not change the sequence of phase precipitation. This study shows that severe plastic deformation has the potential to significantly improve the mechanical properties of age-hardening Al alloys.

1. Introduction

Ultrafine grained (UFG) metals and alloys processed by severe plastic deformation (SPD) techniques have been reported to have superior mechanical properties, such as high strength with good ductility and excellent superplasticity at lower temperature and higher strain rates [1–3]. Among all the SPD techniques, equal channel angular pressing (ECAP) is especially attractive because it can economically produce bulk UFG materials that are 100% dense, contamination free and large enough for real structural applications. [1,2,4,5].

In the last decade, many metals and alloys, including Al and its alloys, Cu, Ni, Ti and its alloys, and steels, have been successfully processed by the ECAP technique. For Al alloys, most ECAP effort has focused on work strengthening Al–Mg alloys [6–9]. Little attention has been paid to precipitate strengthening Al–Zn–Mg 7000 series alloys [10,11], which are widely used for high strength structural applications such as aircrafts and sporting goods. Cold working, which usually improve the strength of metals and alloys, has been found to be ineffective in improving the strength of 7000 series Al alloys [12]. It is of great interest to investigate if the strengthening effect observed in ECAP processed UFG materials can be added to the precipitation hardening effect in the 7000 series Al alloys. If these two strengthening effects can be made additive, it will be possible to significantly improve the strength of 7000 Al alloys, making them much more attractive in high strength structural applications.

It is the objective of this study to investigate the effect of ECAP processing on the mechanical properties and

* Corresponding authors. Tel.: +1-505-665-6774 (Y.H. Zhao), +1-505-667-4029 (Y.T. Zhu); fax: +1-505-667-2264 (Y.T. Zhu).
E-mail addresses: zhao@lanl.gov (Y.H. Zhao), yzhu@lanl.gov (Y.T. Zhu).

precipitation kinetics of the Al–Zn–Mg–Cu 7075 alloy, which is one of the 7000 series Al alloys. The alloy was processed by ECAP immediately after solution treatment to produce a UFG structure, and then naturally aged at room temperature for one month. The microstructures and mechanical properties of the aged UFG 7075 Al alloy and their evolutions during non-isothermal annealing were investigated. The results demonstrate that ECAP processing can enhance the precipitation kinetics and add significant strengthening effect to the precipitation hardening in the 7075 Al alloy.

2. Experimental materials and procedures

2.1. Sample preparation

Commercial 7075 Al alloy rods with a diameter of 20 mm were treated at 480 °C for 5 h to form a solid solution with an initial grain size of approximately 40 μm, and then quenched to room temperature. The Al alloy contains (in wt%) 5.60% Zn, 2.50% Mg, 1.60% Cu, 0.50% Fe, 0.40% Si, 0.30% Mn, 0.23% Cr, and 0.20% Ti.

The ECAP processing was carried out immediately after quenching using a die with an intersecting channel angle of 90° and an outerarc angle of 45°. This die configuration imposes an effective strain of approximately one per ECAP pass [13]. The sample was processed for two passes by route B_c in which the work piece was rotated 90° along its longitudinal axis after the first pass. The ECAP-processed UFG and initial solution treated coarse grained (CG) 7075 Al alloys were naturally aged at room temperature for one month, then were cut into small pieces in an orientation perpendicular to the pressing direction. The surfaces of these thin pieces were polished for subsequent characterizations.

2.2. Thermal analysis

Thermal analysis was performed in a Perkin–Elmer differential scanning calorimeter (DSC-7). Polished alloy disks with a diameter of 5 mm were sealed in Al pans and heated in a flowing Ar atmosphere at a constant heating rate of 5 or 10 °C/min. Two DSC runs were successively performed on each sample with the curve from the second run used as the baseline. To measure the property and microstructure evolutions, the samples were heated to exothermic and endothermic peak temperatures and post peak temperatures and then quenched to room temperature at a cooling rate of 400 °C/min.

2.3. Microstructure and property characterizations

Tensile tests were carried out using a Shimadzu Universal Tester. The samples were cut and polished into a 2.0 mm × 1.4 mm cross-section and a gauge length of 18.0 mm for tensile tests at a displacement rate of 1×10^{-2} mm/s. Microhardness was measured on a Buehler Micromet® Hardness Tester with a load of 500 g and a loading time of 15 s. The indenter is the Vickers diamond pyramid. For each sample, at least 20 points were measured to obtain an average value with a typical uncertainty of ±2%.

Quantitative X-ray diffraction (XRD) measurements were performed with a Scintag X-ray diffractometer, which was equipped with a Cu target operating at 1.8 kW and a graphite curved single-crystal ⟨0 0 0 2⟩ monochromator to select the Cu Kα radiation at the goniometer receiving slit section. The divergence, anti-scattering and receiving slits were chosen to be 0.5°, 0.5° and 0.3 mm, respectively. $\theta - 2\theta$ scans from $2\theta = 10°$ to 143° were performed to record the XRD pattern.

Transmission electron microscopy (TEM) and high-resolution transmission electron microscopy (HREM) were performed using a Phillips CM30 microscope operating at 300 kV and a JEOL 3000F microscope operating at 300 kV, respectively. The TEM and HREM samples were prepared by mechanical grinding of the 7075 Al alloy disks to a thickness of about 10 μm. Further thinning to a thickness of electron transparency was carried out using a Gatan Dual Ion Milling System with an Ar+ accelerating voltage of 4 kV and liquid nitrogen for cooling the specimens.

3. Experimental results

3.1. Thermal analysis

Fig. 1 shows DSC curves from the UFG and CG samples with heating rates of 5 and 10 °C/min. The DSC curves were obtained by subtracting the second scanned baseline from the first scanned DSC curves.

Both UFG and CG samples have an endothermic reaction at lower temperatures (marked as region I), exothermic reactions at intermediate temperatures (region II) including two overlapped peaks (IIA and IIB), and an endothermic reaction at higher temperatures (region III). With increasing heating rate, all the reaction regions moved towards higher temperatures. Comparison with literature data [14–16] indicates that the low temperature endotherm is due to the G–P zones dissolution, the high temperature endotherm is due to the dissolution of the equilibrium hexagonal η phase, and the intermediate region includes the intermediate metastable phase η' and equilibrium phase η formations. However, there are some differences in the DSC curves between the two samples. The first endotherm of the CG sample is broader and the peak temperature is about 25 °C lower than that of the UFG sample. Furthermore, the first endotherm of the CG sample has a shoulder at the end of the peak. The two exothermic peaks of the
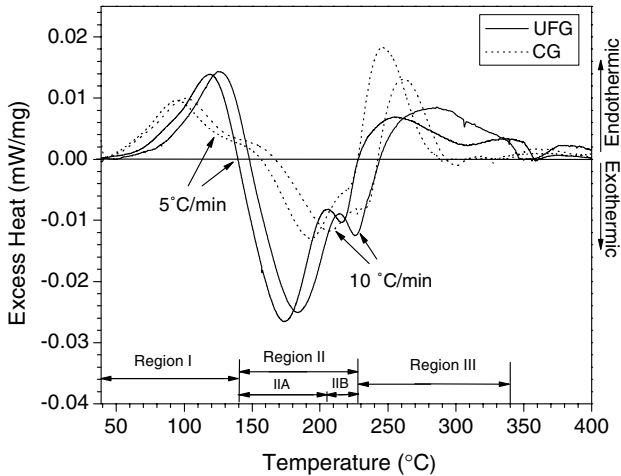
Fig. 1. DSC scans of the UFG (solid lines) and CG (dotted lines) samples with heating rates of 5 and 10 °C/min. The DSC curves were obtained by subtracting the second scanned baseline from the first scanned DSC curves.
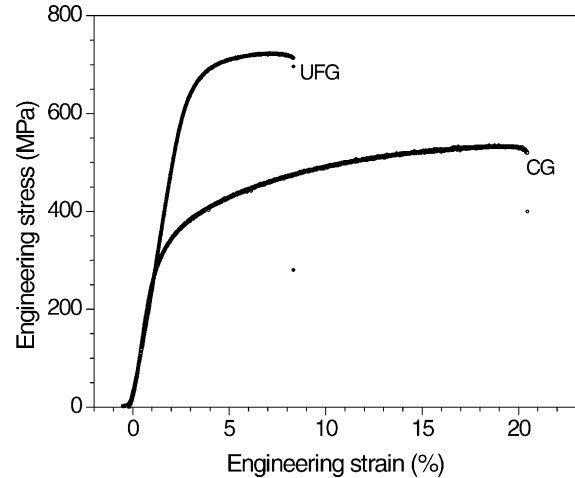

Fig. 2. Tensile engineering stress–strain curves for the UFG (solid circle) and CG (empty circle) samples, both of which were naturally aged for one month.

CG sample overlapped much more than those of the UFG sample. The first exothermic peak temperature of the UFG sample is about 20 °C lower than that of the CG sample. The second endotherm of the UFG sample is much broader than that of the CG sample.

By integrating the areas of the reaction peaks, we obtained the reaction enthalpies, ΔH, as listed in Table 1. For the first endotherm, ΔH of the UFG sample is equivalent to that of the CG sample. For the exotherms and the second endotherm, ΔH of the UFG sample are evidently larger than those of the CG sample.

3.2. Mechanical properties

The engineering stress–strain curves of the UFG and CG samples were shown in Fig. 2. The tensile yield strength and ultimate strength of the UFG sample are 650 and 720 MPa, respectively, which are about 103% and 35% higher, respectively, than those of the CG sample (320 and 530 MPa). The elongation to failure of the UFG sample (8.39%) is smaller than that of the CG sample (20.51%). The present mechanical properties of the CG sample agree well with the literature [17].

The Vickers microhardness evolutions during DSC annealing with heating rates of 5 and 10 °C/min were shown in Fig. 3. The annealing temperatures were selected to correspond to significant temperature regions
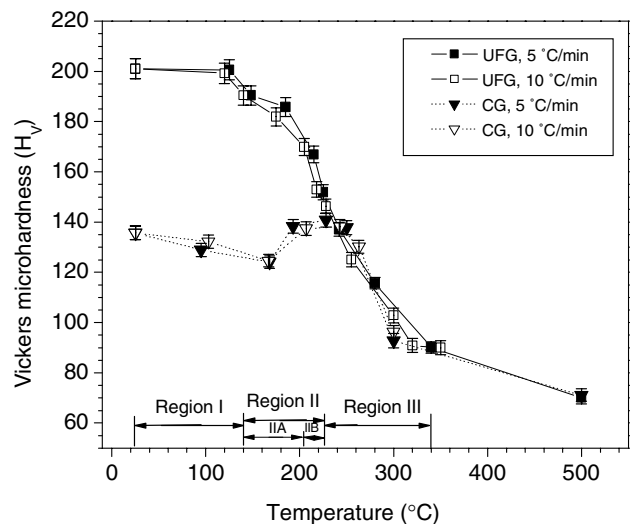

Fig. 3. Vickers microhardness evolutions of the UFG (square symbols) and CG (triangle symbols) samples during DSC annealing with heating rates of 5 (solid symbols) and 10 °C/min (empty symbols). The experimental uncertainty of the microhardness is about ±2% of the hardness value.

in the DSC results shown in Fig. 1. For the UFG sample, the microhardness decreased gradually in regions II and III upon annealing. While for the CG sample, the microhardness decreased at region I, increased at region II, then decreased again at region III. That is, the CG sample has a hardening peak encompassing regions II and III. In region III, the microhardness of the UFG and CG samples have the same decreasing trend. Under the naturally aged condition, the microhardness of the UFG sample is about 48% larger than that of CG sample.

Table 1
The enthalpies, ΔH, of the different reactions during DSC annealing for the UFG and CG samples

ΔH (J/g)	Region I	Region II	Region III
UFG	7.04	−14.27	6.99
CG	6.98	−8.48	4.29

3.3. Microstructures

3.3.1. Phase analysis

The magnified XRD patterns of the UFG and CG samples annealed up to different temperatures with a heating rate of 5 °C/min were shown in Figs. 4(a) and (b). The indexes of diffraction planes of the hexagonal η were also indicated in the figures. The UFG and CG samples have the similar variations in the X-ray patterns during DSC annealing. For the initially aged UFG and CG samples, besides Al reflections, there appeared a broad peak at about $2\theta = 20°$ and some other weak peaks. The broad peak at about 20° corresponds to the G–P zones [18], and the other weak peaks whose positions are a little lower than those of hexagonal η phase
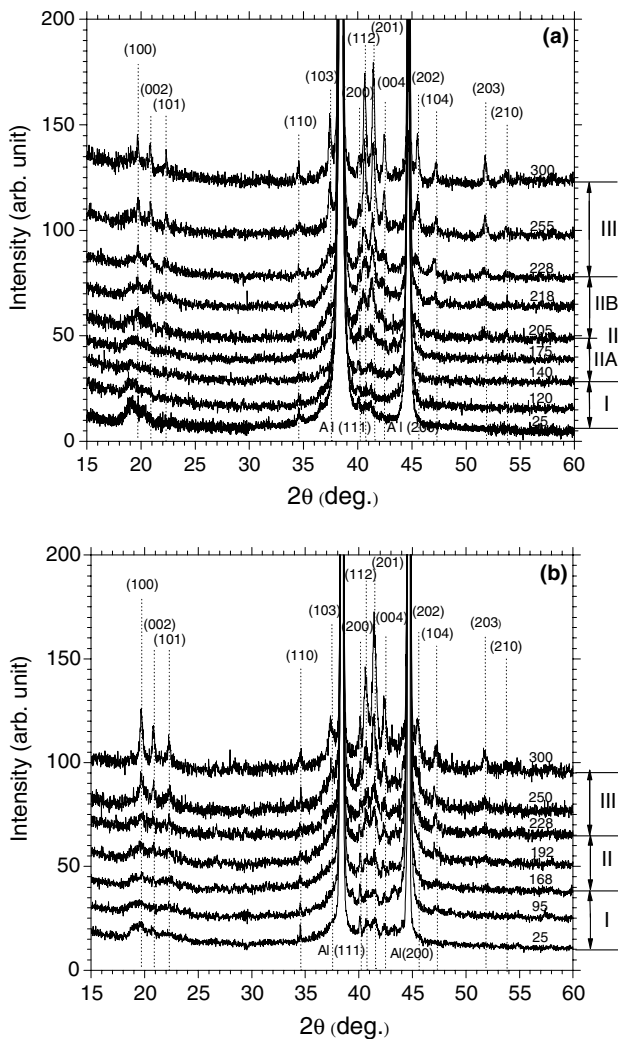

Fig. 4. XRD patterns of the UFG (a) and CG (b) samples annealed up to varying temperatures (as indicated in the figures) with a heating rate of 5 °C/min. The diffraction plane indexes of the hexagonal η phase were indicated in the figures. Region I is corresponding to the dissolution of the G–P zones, region II to the precipitations of the η' and η phases, and region III is corresponding to the coarsening of the η phase.

are from the metastable hexagonal η' phase, whose lattice parameters are a little larger than those of η phase [19]. Because the XRD sample has the same area involved in the reflection, the intensity of the XRD pattern can be compared. Figs. 4(a) and (b) show that the intensity of the G–P zone broad peak of the UFG sample is larger than that of the CG sample, indicating that the volume fraction of the G–P zones in the UFG sample is larger than that in the CG sample. Similarly, XRD patterns indicated the volume fraction of the η' phase in the CG sample is larger than that in the UFG sample.

With increasing annealing temperature in region I, the G–P zone broad peak at about 20° became weaker, indicating the dissolution of the G–P zones. In region IIA, the η' phase was formed, and at the end of region IIA, the intensities of η' peaks (between Al(1 1 1) and (2 0 0) peaks) increased significantly, suggesting the precipitation of a large amount of η' phase. In region IIB, the η' peaks gradually moved towards those of η phase, indicating that part of η' phase gradually transformed into η phase. At the end of region IIB, the little deviation of the peaks to those of η phase indicates that there exists a mixture of η' and η phases. In region III, the precipitates' peaks turned sharper and moved to η phase positions, suggesting all of the η' phase transformed into the η phase and η particles coarsened.

The above-mentioned phase precipitations in the UFG and CG samples can also be observed by TEM and HREM, as shown in Figs. 5(a – e) and 6(a – d), respectively. The HREM pictures were observed from [1 1 0] direction of Al matrix. It was reported that the G–P zones are coherent with the matrix and have a spherical shape (with diameters $\leqslant 7.5$ nm) [20,21]. The semicoherent metastable phase η' phase has a plate shape with a size range of 10–30 nm. The incoherent equilibrium phase η has a needle shape with a size range of 40–80 nm. For the initial naturally aged UFG and CG samples, both the spherical G–P zones (as indicated by arrows in the inset in Fig. 5(a)) and plate-shaped η' phase (see the inset in Fig. 6(a)) are observed. The volume fraction of the G–P zones in the UFG sample is larger than that in the CG sample by numerous observations in different areas, and the volume fraction of η' phase in the CG sample is larger than that in the UFG sample, which agrees with the XRD results.

After the first endotherm (Figs. 5(b) and 6(b)), the amount of G–P zones was reduced significantly, caused by the dissolution of G–P zones. The amount of η' phase decreased slightly, caused by η' dissolution. This suggests that the G–P zone dissolution is the predominant reaction in region I. At 205 °C, corresponding to a temperature at the end of the first exotherm (region IIA), large amount of plate-shaped η' phase precipitated out (Fig. 5(c)). After the second exotherm (region IIB), there appeared large amount of needle-shaped η phase
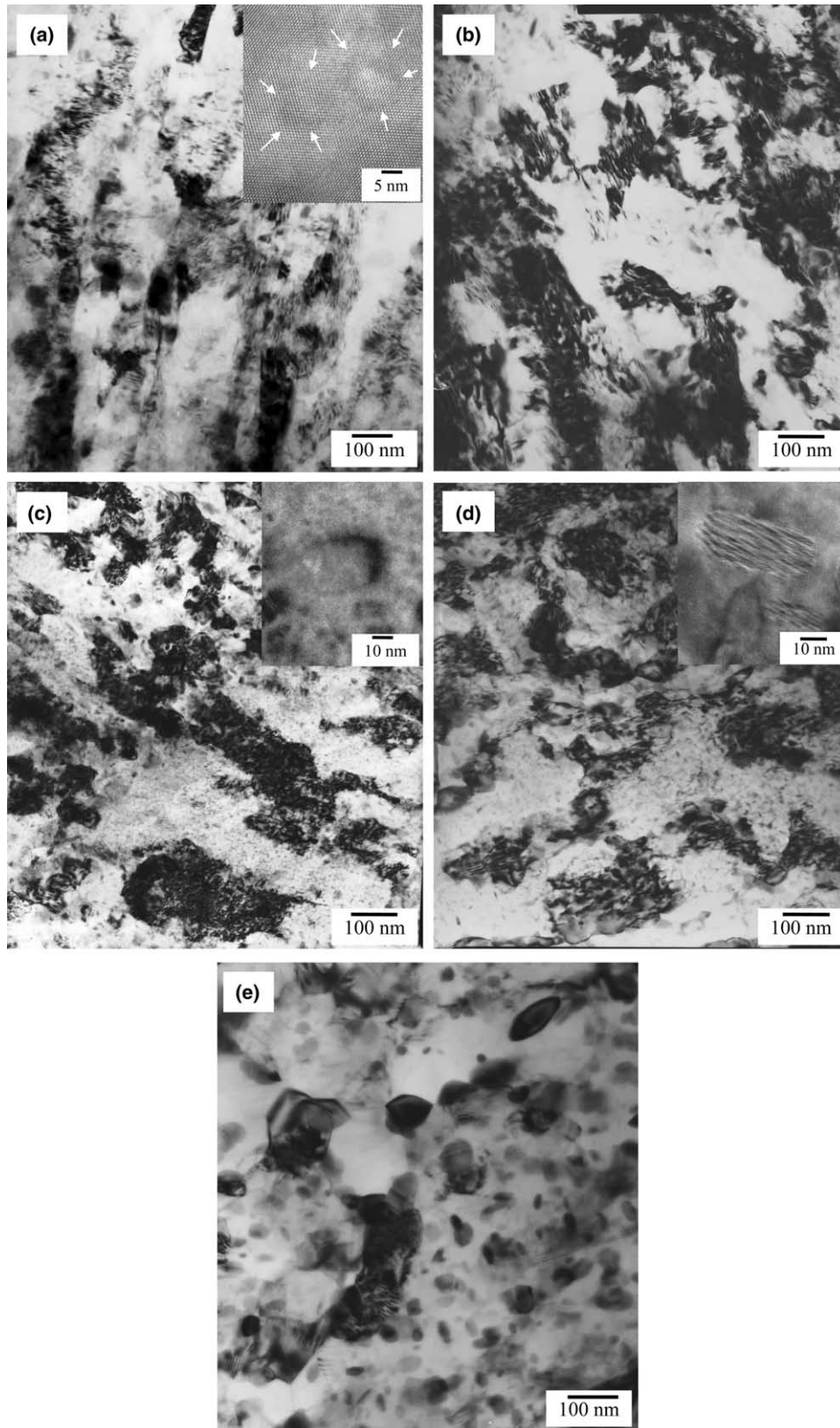
Fig. 5. TEM and HREM pictures of the UFG sample annealed up to different temperatures at a heating rate of 5 °C/min. (a) 25 °C, (b) 140 °C, (c) 205 °C, (d) 228 °C, (e) 300 °C. HREM images of the spherical G–P zones, plate-shaped η' and needle-shaped η phases were shown in the insets in (a), (c) and (d), respectively. The HREM images were observed from [1 1 0] direction of Al matrix.
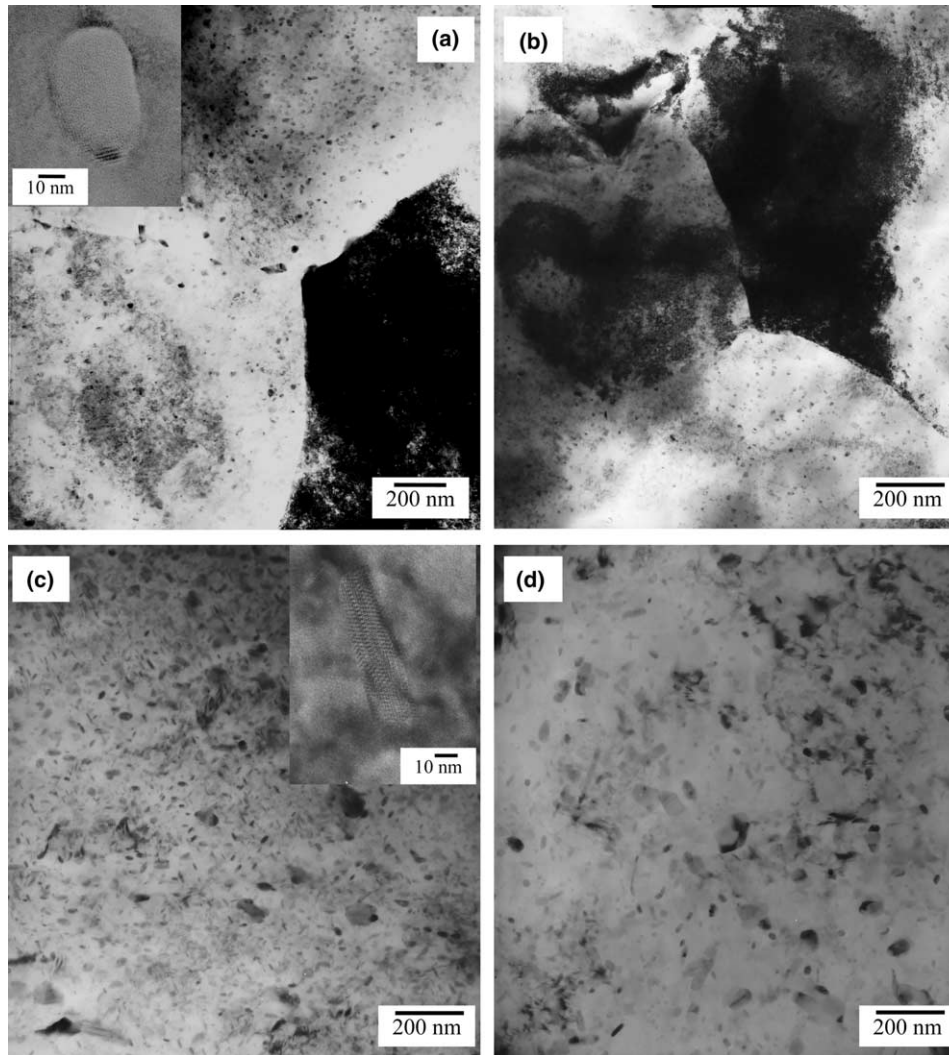
Fig. 6. TEM and HREM images of the CG sample annealed up to different temperatures at a heating rate of 5 °C/min. (a) 25 °C, (b) 168 °C, (c) 228 °C, (d) 300 °C. HREM images of the plate-shaped η' and needle-shaped η phases were shown in the insets in (a) and (c), respectively. The HREM images were observed from [1 1 0] direction.

(40–80 nm) mixed with plate-shaped η' (Figs. 5(d) and 6(c)). At the end of region III, only η needles and coarsened η particles (larger than 100 nm) were observed (Figs. 5(e) and 6(d)).

3.3.2. Texture

Judging from the relative peak intensities in the XRD pattern, we conclude that texture was formed in the UFG 7075 Al alloy. The initially aged UFG sample has a texture with (1 1 1) plane perpendicular to the cylinder axis caused by the ECAP, and upon annealing, the (1 1 1) texture was weakened due to recovery and recrystallization. In the literature, the texture of the ECAP processed UFG materials were found to be related to the detailed pressing geometry [22,23]. The more complete texture measurements (pole figure and orientation distribution function) of the UFG 7075 Al alloy are in progress.

3.3.3. Grain size and microstrain

From TEM images, one can get the grain size statistic distributions and the average grain sizes. Figs. 7(a – c) show some of the grain size (both grain length, D_{length}, and width, D_{width}) histograms for the initial and annealed UFG samples, respectively. We measured over 1000 grains per sample to obtain very good statistics. Grain sizes measured from such histograms are shown in Fig. 8.

The naturally aged UFG sample consists of elongated grains with an average width of about 150 ± 20 nm and a length of about 430 ± 30 nm. This lamella structure was produced by the shear deformation during the ECAP process. By tilting the TEM specimen, the imaged grains changed continuously indicating that the misorientation between neighboring grains are small. This agrees with the TEM observations on ECAP processed Al samples in the literatures [24,25]. When the equiva-
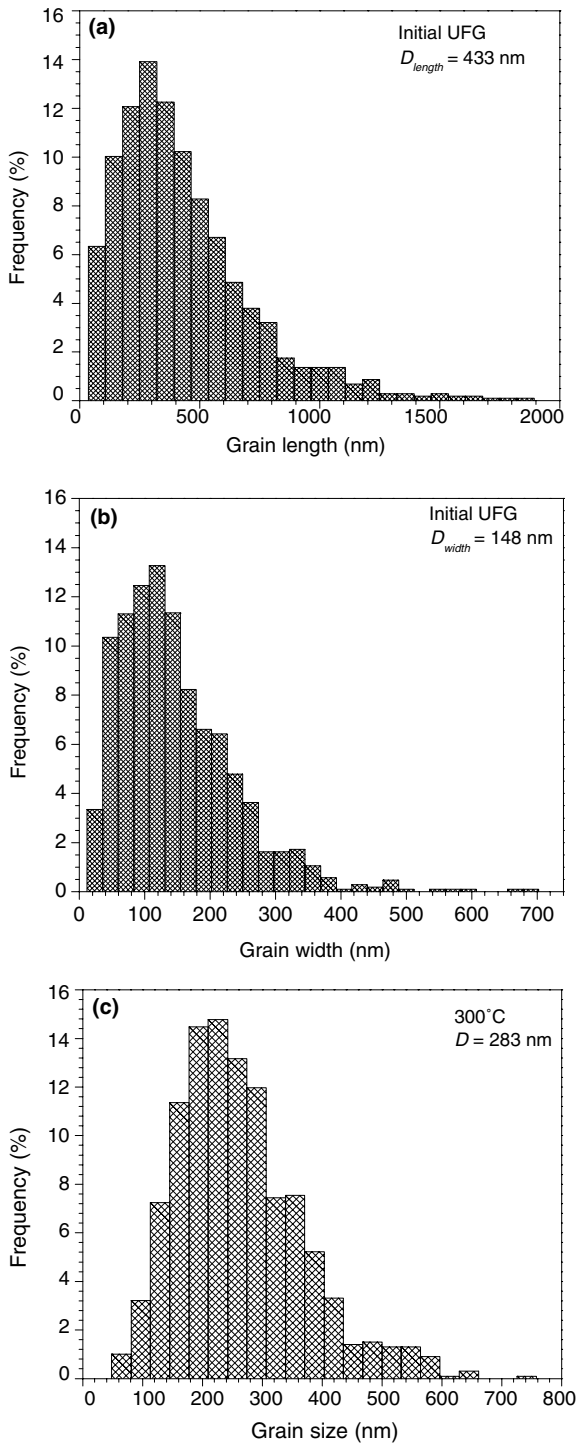
(a) Initial UFG D_{length} = 433 nm

(b) Initial UFG D_{width} = 148 nm

(c) 300 °C D = 283 nm

Fig. 7. Grain size statistic distributions of the initial and annealed UFG samples: (a) grain length, D_{length}, at 25 °C; (b) grain width, D_{width}, at 25 °C; (c) grain diameter after annealing up to 300 °C with a heating rate of 5 °C/min.
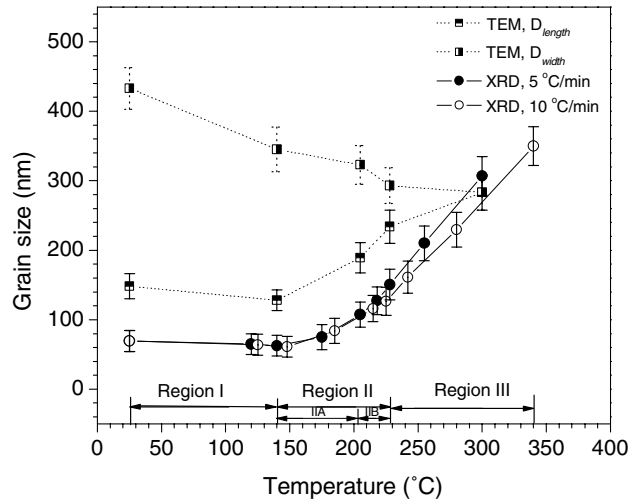

Fig. 8. Grain size evolutions of the UFG sample upon annealing with heating rates of 5 and 10 °C/min, as determined by both X-ray (circles) and TEM (squares) techniques.

with SPD produced structures [26]. The diffuse boundaries are also observed in other ECAP processed UFG materials, and are interpreted by the presence of non-equilibrium boundary configurations [6,27,28]. Studies at higher magnification (HREM) show that the fringes and network within the grains are corresponding to a very high density of dislocations, which are arranged into cell and sub-grain boundaries or form the disloca-
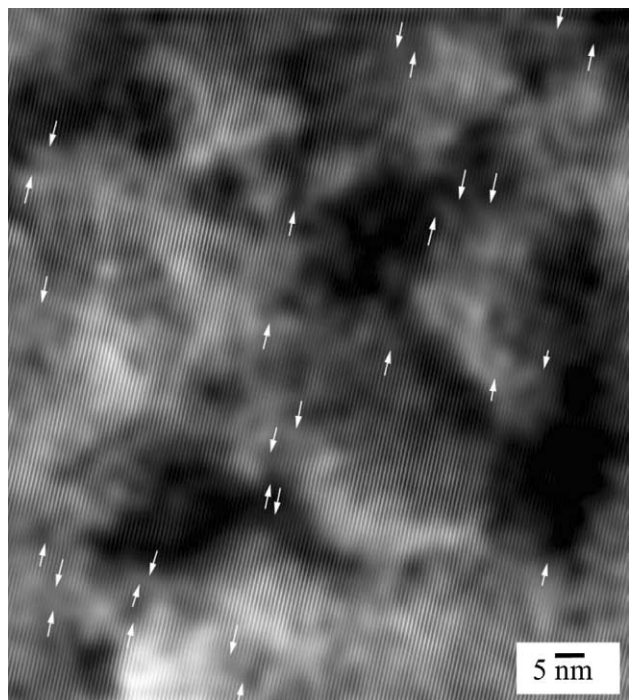

Fig. 9. One-dimensional HREM image of the initially aged UFG 7075 Al alloy. This image was obtained by Fourier and inverse Fourier transformations of the original HREM image. The end of each half atomic plane, which is the core position of a dislocation line, is marked with white arrows.

lent strain was two, the elongated sub-grains are divided by boundaries with low angles of misorientation. As shown in Fig. 5(a), the grain boundaries of the UFG sample are wavy and diffuse. There are many fringes (along both grain length and width directions) and/or network structure within the grains, which is consistent

tion network within the grains, as shown in Fig. 9. The end of each half atomic plane, which is the core position of a dislocation line, is marked with white arrows. The grain size distribution of the UFG sample was non-symmetric with long tail (Figs. 7(a) and (b)), typical of a lognormal distribution [29]. The initial CG sample was composed of equiaxed grains with an average size of about 40 μm. The grain boundaries of the initial CG sample are sharp and straight, corresponding to an equilibrium boundary configuration, as shown in Fig. 6(a).

Annealing up to 140 °C led to slight structural changes, as shown in Fig. 5(b). The grain length and width changed from 430 ± 30 to 345 ± 30 nm and from 150 ± 20 to 130 ± 20 nm, respectively. The reductions of the grain length and width were caused by the formations of grain and sub-grain boundaries from the cell walls by the dislocation rearrangements (recovery) [9]. The existence of many fringes within grains indicated that a high density of dislocations still exist (Fig. 5(b)). Annealing up to 208 °C led to significant dislocation recovery, a slight decrease in grain length to 320 ± 30 nm, and an evident increase in grain width to 190 ± 20 nm, as shown in Figs. 5(c) and 8. Some grains showed a much reduced dislocation density while others retain a high dislocation density. When the UFG sample was annealed up to 228 °C, the grain length decreased to 295 ± 20 nm, and the grain width increased to 235 ± 20 nm. The grains appeared much more equiaxed than in the unannealed UFG state (Fig. 5(d)). Annealing up to 300 °C caused a complete recrystallization (Fig. 5(e)). The whole sample was composed of ultrafine recrystallized equiaxed grains with an average size of about 285 ± 20 nm. The size distribution function was more symmetric, as shown in Fig. 7(c). From TEM, the grain size of the initial CG sample increased from about 40 to 50 μm during DSC annealing.

The average grain size D and microstrain $\langle \varepsilon^2 \rangle^{1/2}$ can be calculated from the XRD peak broadening [30], as shown in Figs. 8 and 10. The grain size D of the UFG sample increased from about 70 ± 15 to 310 ± 30 nm after the DSC annealing to 300 °C. The microstrain of the UFG sample decreased significantly from about $0.50 \pm 0.04\%$ to $0.12 \pm 0.02\%$ in regions II and III. In contrast, the microstrain of the CG sample increased from $0.05 \pm 0.02\%$ to $0.15 \pm 0.02\%$ upon annealing. The grain size from XRD result was smaller than those from TEM, which is because XRD measures the coherent diffraction domain size, which is sub-grain/dislocation cell size [26].

3.3.4. Lattice parameter

Fig. 11 shows the lattice parameter evolutions of the UFG and CG Al alloys during DSC annealing. The lattice parameter was determined from the XRD peak positions. The lattice parameters of the initial aged UFG and CG samples are about 4.056 ± 0.005 Å. This value is about
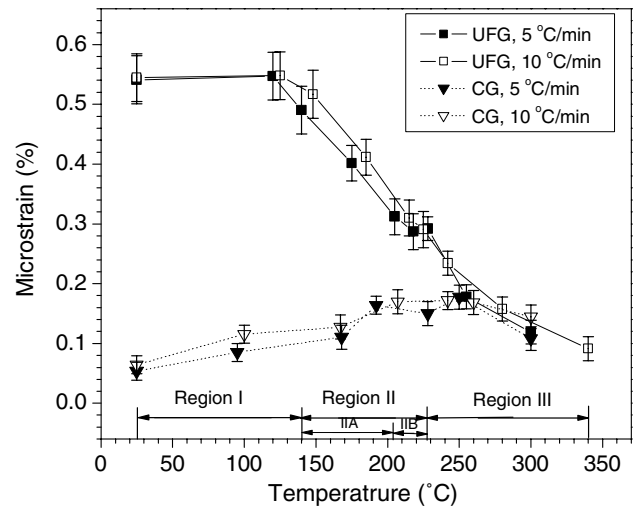

Fig. 10. Microstrain evolutions of the UFG (squares) and CG (triangles) samples during annealing with heating rates of 5 (solid symbols) and 10 °C/min (empty symbols), as determined by XRD peak broadening analysis [30].
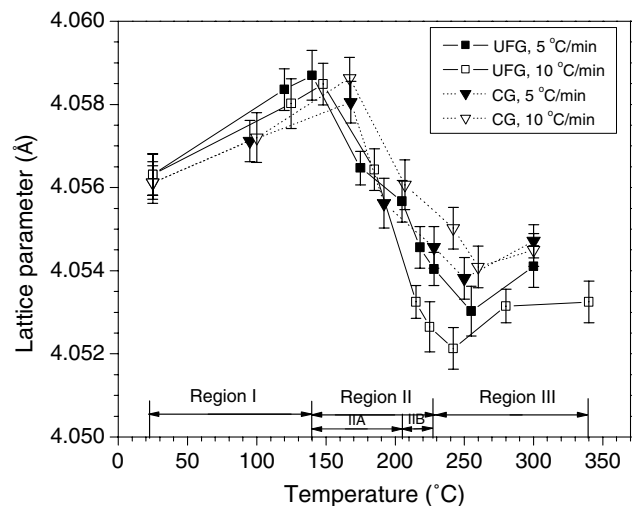

Fig. 11. Evolutions of lattice parameters of the UFG (squares) and CG (triangles) samples during DSC annealing with heating rates of 5 (solid symbols) and 10 °C/min (empty symbols), as determined from the XRD peak positions.

0.17% larger than the lattice parameter of pure Al (4.0494 Å [31]). Upon annealing, the lattice parameters of the UFG and CG samples have similar changes: increased to about 4.059 ± 0.005 Å in region I, and decreased significantly in region II, then increased again slightly in region III. These variations can be explained by G–P zone dissolution in region I, η', η precipitation in region II, and η dissolution in region III. The dissolution of Mg and Zn etc. into Al matrix increases the Al lattice constant, the reverse process decreases Al lattice constant.

3.3.5. Dislocation density

The HREM revealed large amount of dislocations both at the grain/sub-grain boundaries and within the
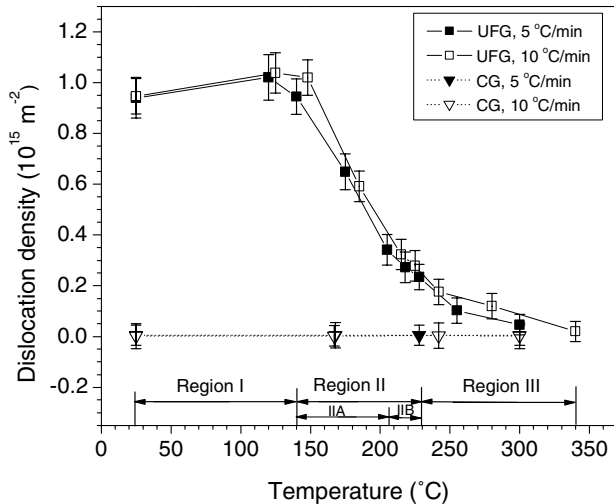
Fig. 12. Dislocation density evolutions of the UFG (squares) and CG (triangles) samples during DSC annealing with heating rates of 5 (solid symbols) and 10 °C/min (empty symbols), as determined from the grain size and microstrain [32,33].

grains of the UFG sample (Fig. 9). For the materials subjected to severe plastic deformation, dislocations density ρ can be represented in terms of grain size D and microstrain $\langle \varepsilon^2 \rangle^{1/2}$ by [32,33]:

$$\rho = 2\sqrt{3}\langle \varepsilon^2 \rangle^{1/2}/(D * b), \qquad (1)$$

where b is the Burgers vector and equals to $\sqrt{2}a/2$ for an fcc Al alloy. The calculated ρ in the UFG and CG samples was shown in Fig. 12. The ρ of the UFG sample is found to be $(0.94 \pm 0.08) \times 10^{15}$ m^{-2}, and has no change when annealing up to 140 °C, agreeing with the TEM observation (Fig. 5(b)). Annealing up to 205 °C led to a significant reduction of the ρ from $(0.95 \pm 0.08) \times 10^{15}$ to $(0.34 \pm 0.06) \times 10^{15}$ m^{-2}. The further annealing up to 228 °C reduced the ρ further to $(0.23 \pm 0.05) \times 10^{15}$ m^{-2}, in agreement with the TEM results (Figs. 5(c) and (d)). When annealed to 300 °C, where complete recrystallization occurred, the ρ decreased to about $(0.05 \pm 0.04) \times 10^{15}$ m^{-2}. For the CG sample, the ρ remained at ∼0 during annealing.

4. Discussion

4.1. Phase precipitation kinetics

The normal precipitation sequence of 7075 Al alloy during aging of the supersaturated solid solution is [19–21]:

Supersaturated solid solution

$\rightarrow$ Guinier–Preston (G–P)zones $\rightarrow \eta'(\text{MgZn}_2)$

$\rightarrow \eta(\text{MgZn}_2)$

The interfacial energy between G–P zones and the matrix is very low and a high density of very small size G–P zones can usually form at room temperature. The semicoherent intermediate metastable phase η' nucleates and grows from the G–P zones. The incoherent equilibrium phase η grows from η' phase. The experimental results from DSC, X-ray and TEM indicate that ECAP only changed the kinetics of precipitate phases formation, without changing their sequence.

The higher volume fraction of the G–P zones and lower volume fraction of η' phase in the naturally aged UFG sample than those in the naturally aged CG sample indicate that the ECAP process accelerates the precipitation of G–P zones, but suppresses the formation and growth of the η' phase. Moreover, the higher peak temperature of the G–P zones dissolution in the UFG sample than that of the CG sample indicates that the G–P zones in the UFG sample is more stable than that in the CG sample. The broad shoulder at the end of the G–P zone dissolution peak in the CG sample was caused by the dissolution of η' phase [14]. In addition, the lower peak temperature of η' formation in the UFG sample than that in the CG sample also indicate that the ECAP process accelerates the phase precipitations.

The much larger enthalpy of region II of the UFG sample than that of the CG sample could be caused by the defects recovery and/or the heavy phase precipitation. To separate these two contributions, we calculated the energy of defect (dislocations) recovery in region II. The detailed calculation procedures were described in [34,35]. The energy of defect recovery was determined to be about 0.3 J/g, which account for only a very small fraction of ΔH. This suggests that the large ΔH in region II originates from the formation of large volume fractions of precipitates. This result also verifies that the ECAP process accelerates the precipitation. The larger enthalpy of η dissolution of the UFG sample than that of the CG sample can be explained by the precipitation of larger volume fraction of η phase in region II.

4.2. Mechanical properties and strengthening mechanisms

The strength of the naturally aged UFG 7075 alloy is significantly higher than its naturally aged CG counterparts, indicating that it is possible to add the strengthening effect from ECAP processing to that from the precipitation hardening. In the literature, the thermo-mechanical treatment (combining deformation and heat treatment) only increases the yield stress and ultimate stress of 7075 Al alloy to about 550 and 600 MPa, respectively [17], which is much smaller than that of the naturally aged UFG 7075 alloy in this study.

The significantly high strength of the UFG 7075 Al alloy may be attributed to: (i) solid solution strengthening, (ii) grain refinement strengthening, (iii) dislocation strengthening and (iv) precipitation strengthening.

Solid solution strengthening originates from the elastic distortions produced by substitutional atoms (such as Zn, Mg Cu, Fe) in the Al matrix. The lattice parameter of 7075 Al alloy is a measure of the solid solubility, and therefore a measure of the solid solution strengthening. In present experiment, the lattice parameter of the UFG sample has similar variation against annealing with that of the CG sample. Therefore, the solid solution strengthening is not the main contributor to the high strength of the UFG sample. The grain refinement strengthening is generally described by a Hall–Petch equation [36,37]. Because in region III, both the UFG and CG samples have the same microhardness even though their grain sizes are very different, the grain refinement is not a main contributor either. This can be understood by the fact that most grain boundaries present after a strain of about two by ECAP process are dislocation walls or sub-boundaries with low angles of misorientation, not real high angle boundaries, as stated in Section 3.3.3.

The XRD and HREM analyses revealed high dislocation density in the initial naturally aged UFG sample, suggesting that the dislocation strengthening has significant contribution to the strength enhancement. The dislocation networks and tangles within grains and near grain or sub-grain boundaries make dislocation glide more difficult. The precipitation strengthening results from the precipitate's ability to impede dislocation motion by forcing dislocations to either cut through or circumvent the fine precipitates. In either case, higher density of precipitates leads to higher strength. For naturally aged 7075 Al alloy, the dislocation cutting of the G–P zones and η' fine plates is the main strengthening mechanism, because the strong atomic bonds in the zones can effectively hinder dislocation motion [38–40]. Both XRD and HREM revealed that the volume fraction of the G–P zones in the UFG sample is larger than that in the CG sample. Therefore, the cooperative interaction of the high densities of the G–P zones and dislocations has resulted in the observed significantly higher strength of the UFG 7075 Al alloy.

The hardening peak of the CG sample in region II is caused by the formation of the η' phase. For the UFG sample, the hardening peak in region II disappeared because the dislocation density decreased significantly in region II and overcompensated the η' hardening.

4.3. Thermal stability

During the annealing of the UFG 7075 Al alloy at a constant rate of 5 °C/min, the recrystallization started at 228 °C and completed at 300 °C, indicating a high thermal stability which is believed to be related to the precipitated η' and η phases. As shown in Fig. 5(e), there are many η particles at the grain boundaries, and these particles will pin the grain boundaries and therefore retain the fine grain sizes up to considerably higher temperatures.

5. Conclusions

A combination of SPD processing and precipitation hardening has the potential to render Al 7000 series alloys significantly stronger than those processed by either technique alone. The high density of G–P zones and dislocations are primarily responsible for the high strength of naturally aged UFG 7075 alloy. During annealing, there exists a hardening peak for the CG sample caused by the formations of the η' phase. For the UFG sample, the hardening peak was lost due to the significant, simultaneous decrease in dislocation density. The ECAP process accelerated the phase precipitation kinetics, but did not change the sequence of phase precipitation. The UFG 7075 Al matrix shows a high thermal stability caused by the pinning effect of the numerous precipitates at the grain boundaries.

References

[1] Valiev RZ, Alexandrov IV, Zhu YT, Lowe TC. J Mater Res 2002;17:5.
[2] Valiev RZ, Islamgaliev RK, Alexandrov IV. Prog Mater Sci 2000;45:103.
[3] Matsubara K, Miyahara Y, Horita Z, Langdon TG. Acta Mater 2003;51:3073.
[4] Furukawa M, Horita Z, Nemoto M, Langdon TG. J Mater Sci 2001;36:2835.
[5] Zhu YT, Lowe TC. Mater Sci Eng 2000;A291:46.
[6] Wang J, Iwahashi Y, Horita Z, Furukawa M, Nemoto M, Valiev RZ, et al. Acta Mater 1996;44:2973.
[7] Furukawa M, Utsunomiya A, Matsubara K, Horita Z, Langdon TG. Acta Mater 2001;49:3829.
[8] Lee S, Utsunomiya A, Akamatsu H, Neishi K, Furukawa M, Horita Z, et al. Acta Mater 2002;50:553.
[9] Morris DG, Munoz-Morris MA. Acta Mater 2002;50:4047.
[10] Horita Z, Fujinami T, Nemoto M, Langdon TG. Metall Trans A 2000;31A:691.
[11] Zheng LJ, Chen CQ, Zhou TT, Liu PY, Zeng MG. Mater Character 2003;49:455.
[12] Smith WF, editor. Structure and properties of engineering alloys. New York: McGraw-Hill; 1993. p. 214 [Chapter 5–9].
[13] Iwahashi Y, Wang Y, Horita Z, Nemoto M, Langdon TG. Scripta Mater 1996;35:143.
[14] Deiasi R, Adler PN. Metall Trans A 1977;8A:1177.
[15] Adler PN, Deiasi R. Metall Trans A 1977;8A:1185.
[16] Papazian JM. Metall Trans A 1982;13A:761.
[17] Murakami Y. Aluminum-based alloys. In: Cahn RW, editor. Processing metals and alloys. Weinheim, New York: VCH; 1991. p. 253.
[18] Zhao YH, Liao XZ, Jin Z, Valiev RZ, Zhu YT. Structure and property evolutions of ECAPed 7075 Al alloy during annealing. In: Zhu YT, Langdon TG, Valiev RZ, Semiatin SL, Shin DH, Lowe TC, editors. Ultrafine-grained materials III. The Minerals, Metals and Materials Society; 2004. p. 511.
[19] Mondolfo LF, Gjostein NA, Levinson DW. Trans Am Inst Min (Metall) Engrs 1956;206:1378.

[20] Thomas G, Nutting J. J Inst Met 1959–60;88:81.
[21] Embury JD, Nicholson RB. Acta Metall 1965;13:403.
[22] Pithan C, Hashimoto T, Kawazoe M, Nagahora J, Higashi K. Mater Sci Eng 2000;A280:62.
[23] Cui Q, Ohori K. J Jpn Inst Light Met 1999;49:155.
[24] Iwahashi Y, Horita Z, Memoto M, Langdon TG. Acta Mater 1998;46:3317.
[25] Iwahashi Y, Horita Z, Memoto M, Langdon TG. Acta Mater 1997;45:4733.
[26] Zhu YT, Huang JY, Gubicza J, Ungár T, Wang YM, Ma E, Valiev RZ. J Mater Res 2003;18:1908.
[27] Huang JY, Zhu YT, Jiang H, Lowe TC. Acta Mater 2001;49:1497.
[28] Huang JY, Liao XZ, Zhu YT, Zhou F, Lavernia EJ. Philos Mag 2003;83:1407.
[29] Alexandrov IV, Zhu YT, Lowe TC, Islamgaliev RK, Valiev RZ. Metall Mater Trans 1998;29A:2253.
[30] Zhao YH, Zhang K, Lu K. Phys Rev 1997;B56:14322.
[31] Powder diffraction file, No. 04-0787, Swarthmore, PA: Joint Committee on Powder Diffraction Standards (JCPDS) 1990.
[32] Williamson GK, Smallman RE. Philos Mag 1956;1:34.
[33] Smallman RE, Westmacott KH. Philos Mag 1957;2:669.
[34] Zhao YH, Zhang K, Lu K. Phys Rev 2002;B66:085404-01.
[35] Zhao YH, Sheng HW, Lu K. Acta Mater 2001;49:365.
[36] Hall EO. Proc Phys Soc 1951;B64:747.
[37] Petch NJ. J Iron Steel Inst 1953;174:25.
[38] Adler PN, Delasi R, Geschwind G. Metall Trans A 1972;3:3191.
[39] Staley JT. Metall Trans A 1974;5:929.
[40] Kelly A, Nicholson RB. Prog Mater Sci 1963;10:216.